CHEMISTRY OF MATERIALS

Open Access

pubs.acs.org/cm

Article

Guest-Induced Flexibility in a Multifunctional Ruthenium-Based Metal−Organic Framework

Karen D. J. Hindricks, Volodymyr Bon,* Oliver Treske, Adrian Hannebauer, Andreas Schaate, Yaşar Krysiak,* and Stefan Kaskel

Cite This: *Chem. Mater.* 2024, 36, 657−665

Read Online

ACCESS | Metrics & More | Article Recommendations | Supporting Information

ABSTRACT: We present a new example of rare metal−organic frameworks (MOFs) containing ruthenium inorganic building units (IBUs). Advanced characterization techniques such as three-dimensional electron diffraction and *in situ* powder X-ray diffraction, performed in parallel with adsorption of various gases and vapors, were used to determine the structure and framework dynamics of $[Ru_2(bzpdc)(bipy)]$ (*bzpdc* = 4,4′-benzophenone dicarboxylate, *bipy* = 4,4′-bipyridine), revealing unique and highly relevant material features: In the 2D nanoporous framework, ruthenium paddle-wheel IBUs are mixed-valent and provide potential open metal sites. Coupled with the flexible behavior of the framework in the form of specific reversible structural transformations and selective gating upon adsorption of various guests, the material is thus ideally suited for sensing or catalytic applications.

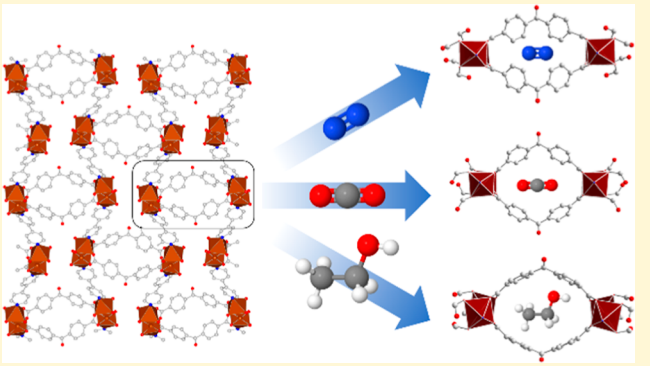

INTRODUCTION

Metal−organic frameworks (MOFs) are an emerging class of nanoporous materials with multifunctional properties going far beyond other ordered micro- and mesoporous inorganic compounds.[1−6] This is particularly true for soft porous crystals - MOFs with a flexible framework, responding to physical or chemical stimuli with a reversible structural transformation.[3,7−9] MOFs' reticular design from inorganic building units (IBUs) and bridging organic linkers provides a high synthetic tunability and structural regularity.[10] Inorganic and organic components can be hierarchically integrated into a single porous material to implement structure−function relationships for specific applications.[6] Including but not limited to gas separation and storage,[11−14] catalysis and sensing.[15−19]

Due to its diverse redox chemistry, ruthenium is a very versatile element, and its compounds have long been established in highly demanded fields. Ranging from the catalysis of organic transformations,[20,21] redox processes such as the conversion of CO_2 and water-oxidation,[22−24] to use as photosensitizers in solar cells or in cancer therapy.[25,26] Combining ruthenium species with functional nanoporous metal−organic frameworks holds the potential to solve existing problems such as poor recyclability or deactivation and the accessibility of reactive Ru-centers.[27,28] By exploitating the multifunctionality and specific structure−function relationships of MOFs, high-performance materials could be synthesized. However, despite the very rich coordination chemistry of ruthenium,[29] the incorporation of precious group metals into MOFs as the structure-determining components remains challenging.[30] As a result, there are hardly any examples of MOFs featuring Ru-IBUs among the well over 100,000 MOF compounds already published.[31,32] The most prominent example is mixed valence $[Ru_3^{II,III}(btc)_2(Cl_{1.5})]$, a structural analogue to HKUST-1, first published by Fischer *et al.* in 2011.[33] In addition to further synthesis development[34] and extensive characterization,[35] (Ru)HKUST-1 was optimized for catalytic applications.[36−39] Moreover, a $Ru^{II,II}$ analog MOF,[40] as well as mixed Ru/Rh-derivatives $[Ru_xRh_{3-x}(btc)_2]$ were successfully synthesized.[30] To the best of our knowledge, only one other MOF family providing Ru-IBUs has been reported to date. Lin and co-workers designed two MOFs based on Ru_2 paddle-wheel IBUs and porphyrin-derived tetracarboxylate ligands for the visible-light-driven hydrogen evolution reaction.[41]

In the following, we introduce a new representative of rare Ru-IBU MOFs. The mixed-linker MOF $[Ru_2(bzpdc)(bipy)]$ (*bzpdc* = 4,4′-benzophenone dicarboxylate, *bipy* = 4,4′-bipyridine) provides dual functionality. (1) The Ru paddle-wheel IBUs are mixed-valent and are not completely saturated by the linker molecules, thus providing potential open metal sites (OMS).[28]

Received: July 26, 2023
Revised: December 13, 2023
Accepted: December 13, 2023
Published: January 3, 2024

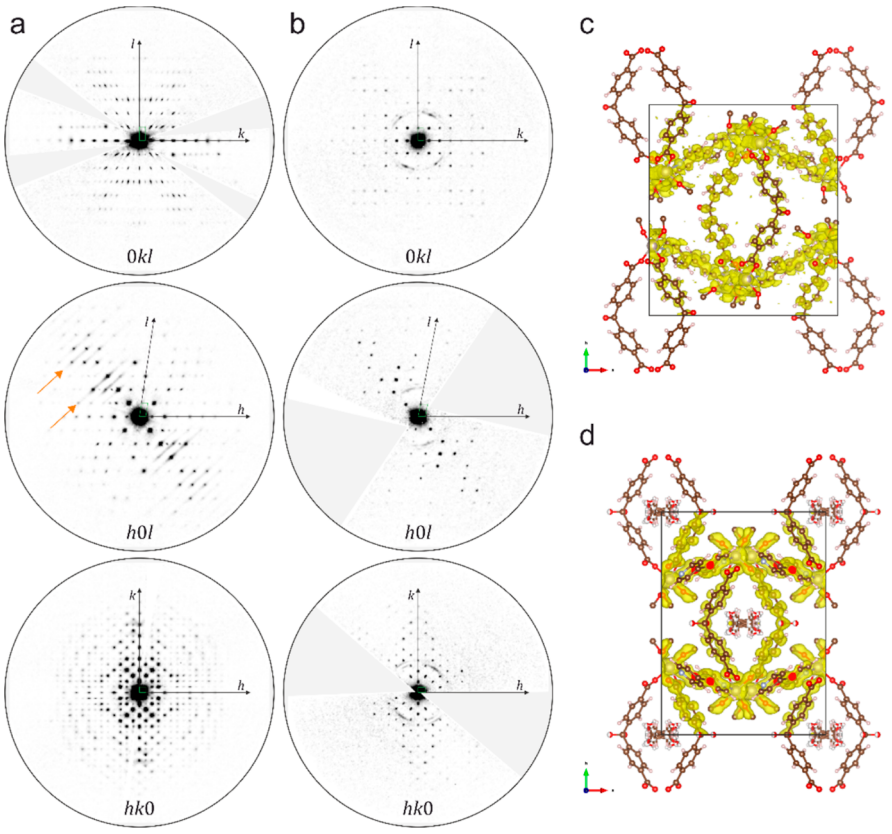

Figure 1. 3D ED patterns of Ru-MOF, reconstructed from the individual measured frames. (a) Ru-MOF measured at RT and (b) EtOH@Ru-MOF-I, measured at −180 °C. The orange arrows indicate diffuse streaks in section *h*0*l*. (c,d) Result of *ab initio* structure solution plotted using VESTA. Potential maps $V(\boldsymbol{r})$ based on structure solution performed in Superflip for (c) Ru-MOF np phase and (d) EtOH@Ru-MOF-I. Transparent yellow potentials are plotted using the $2\sigma[V(\boldsymbol{r})]$ threshold (σ is the standard deviation of map values). Scattering density is superimposed with refined crystal structures presented as a ball and stick model.

(2) The *bzpdc* linker implements photoactivity, the possibility of easily accessible postsynthetic modifications, and even spatially resolved micropatterning.[42−47] Coupled with the flexible behavior of the MOF and specific reversible structural transformations upon adsorption of various guests, the material constitutes an ideal platform for sensing or catalytic applications. Advanced techniques such as three-dimensional electron diffraction (3D ED) and *in situ* XRD measurements during fluid physisorption elucidate the flexible structure and adsorption properties of the novel material.[48,49]

RESULTS AND DISCUSSION

$[Ru_2(bzpdc)(bipy)]$ is obtained via solvothermal synthesis from DMF as a light-yellow crystalline powder (detailed description of the synthesis in the Supporting Information, Section S1.3). Images taken on a digital light microscope show star-shaped crystals with a size of up to 40 μm (Figure S12, Supporting Information). Each crystal consists of eight intergrown individuals. In vacuum, the crystals break, which is why only fragments can be seen in the SEM images (Figure S12, Supporting Information). A look into the fracture edges of the crystals reveals that they are hollow on the inside. Hollow MOF micro- and nanostructures are attracting huge research interest in recent years and have been widely adopted as spatially confined reactors for various applications.[50] We assume a self-templated mechanism during the solvothermal synthesis, whereby an intermediate product spontaneously transforms into the hollow MOF structure.[51] However, the synthesis mechanism seems to be more complicated and requires a more elaborate study that goes beyond this publication. In this work, we focus on the structural analysis and dynamic sorption properties of the new material.

Structure Description. As a consequence of the intergrown crystals of Ru-MOF, structure determination by conventional single-crystal X-ray diffraction (SCXRD) methods is hardly possible. Moreover, it was impossible to index the PXRD data due to broadened and overlapping reflections. Therefore, three-dimensional electron diffraction (3D ED) using a transmission electron microscope (TEM) was invoked because it allows structural analysis of crystals down to the nanoscale and has proven to be a very valuable tool for determining crystal structures from small MOF crystals.[48,52]

Various fist-wedge-shaped particles (Figure S3, Supporting Information) were measured at room- and cryogenic temperatures in a ultrahigh vacuum under low illumination conditions (for further details, see Supporting Information Section S2.1). The reconstruction of six 3D ED data sets led to a monoclinic unit cell [a = 18.934(2) Å, b = 20.912(3) Å, c = 8.702(1) Å, β = 98.35(1), and space group $P2_1/a$]. The sample shows, in general, a strongly preferred orientation of the crystals on the carbon film of the TEM grid. The longest b axis is perpendicular to the TEM grid, from which it can be concluded that the short side of the anisotropic crystals is related to the ***b***-direction of the crystal lattice. Crystal growth seems to be favored in the ***a***- and ***c***-directions. Furthermore, it is noticeable that all measured crystals show a very similar pattern of diffuse scattering (Figures

https://doi.org/10.1021/acs.chemmater.3c01845
Chem. Mater. 2024, 36, 657−665

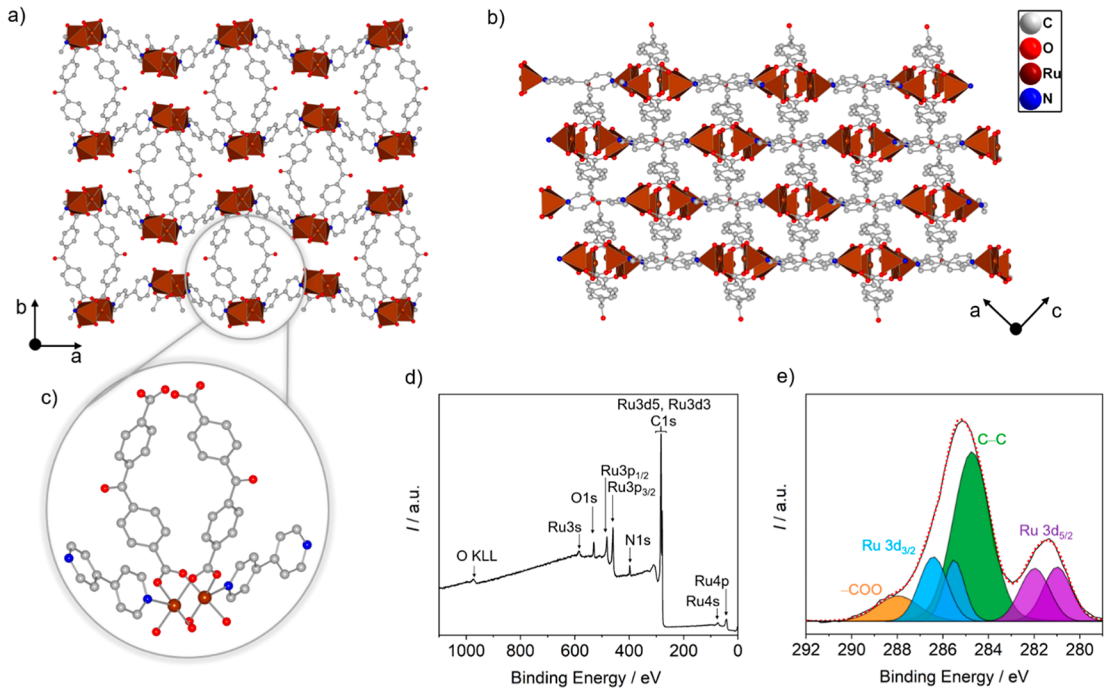

Figure 2. Crystal structure of Ru-MOF obtained from 3D ED and PXRD data. (a) Structure of Ru-MOF plotted with a view along the *c*-axis and (b) along the *b*-axis. (c) Coordination environment of a paddle-wheel IBU. Hydrogen atoms are omitted for clarity. (d) XP survey scan and (e) deconvoluted XP spectrum of the Ru-MOF C 1s region.

1a, S4). The diffuse scattering is independent of the temperature and, therefore, appears to be static in nature. However, diffuse scattering was ignored for intensity integration. To increase the completeness of the data, data sets of different crystals, including the rare orientation (***b***-axis parallel to the grid), had to be combined. A scattering map with atomic resolution led to a chemically reasonable initial structure model, [Ru_2(*bzpdc*)-(*bipy*)] (Figure 1c). The structural model could only be refined to a limited extent, possibly due to the strong crystal imperfections. Therefore, the crystal structure was further completed and refined using PXRD data (measured under ambient conditions; for further details, see Supporting Information Section S2.2).

Figure 2 shows the crystal structure of Ru-MOF. Ruthenium paddle-wheel IBUs define the nodes of the network. Paddle wheels are a common structural motif in MOFs[53] and are also present in the two known Ru-based MOFs.[33,41] In [Ru_2(*bzpdc*)-(*bipy*)], each paddle wheel is coordinated axially by two *bipy*-linkers and equatorially by two *bzpdc*-linkers (Figure 2c). Thus, the paddle wheels are bridged by *bipy* to form 1D corrugated chains, which are pillared by the *bzpdc* ligands perpendicular to form 2D layers (Figure 2a). Offset stacking along the diagonal drawn by the *a*- and *c*-axes results in a supramolecular 3D network (Figure 2b). The stacking causes smaller channels perpendicular to the layers but also creates 1D channels along the *c*-axis. Two IBUs are each bridged by two *bzpdc* linkers. The other equatorial side of the IBU is not saturated by linkers, suggesting coordination of charge balancing and neutral species such as OH^-, Cl^-, COO^-, or H_2O. It is known that charge-neural terminal ligands can be removed by vacuum or thermal treatment, exposing reactive open metal sites (OMS).[28] The superordinate topology of the MOF is preserved, and the resulting OMS can act as typical Lewis acid sites.[28] While the generation of OMS in [Ru_2(*bzpdc*)(*bipy*)] introduced here remains to be investigated in follow-up studies, in (Ru)HKUST-1, analogous OMS were already obtained by defect engineering and led to improved properties in catalysis and CO sorption.[36] This opens up exciting possibilities for research and application.

The UV−vis spectrum of the Ru-MOF (Figure S13, Supporting Information) is characterized by two broad bands from the benzophenone moiety. A $n-\pi^*$ band in the range of 320−370 nm and a band in the range of 240−300 nm correspond to several $\pi-\pi^*$ transitions.[54] The band around 425 nm can be attributed to the characteristic absorption peak due to the d−d transition in the ruthenium metal ions of the framework, consistent with its light yellow color. In order to elucidate the oxidation state of the Ru centers, high-resolution X-ray photoelectron spectroscopy (XPS) studies were carried out (Figure 2d,e). The Ru 3d peaks in the XP spectrum (Figure 2e) were dominated by two main spin orbit components: Ru $3d_{5/2}$ (280−284 eV) and Ru $3d_{3/2}$ (284−288 eV). Two different Ru species can be identified: Ru^{II} at 282 and 286 eV, as well as Ru^{III} at 281 and 285 eV. These findings are in line with XPS data from mixed-valence Ru-HKUST.[33] Mixed-valence $Ru^{II,III}$ paddle wheels are not uncommon and were also observed in (Ru)HKUST-1, among others.[33] Fundamentally, mixed valency gives rise to redox activity and electrical conductivity.[55,56] The intense hydrocarbon C 1s peak at 285 eV and the carboxylate (−COO) C 1s peak at 288 eV further characterize the Ru-MOF structure. In addition, the corresponding XP survey data (Figure 2d) display a N 1s peak at about 399 eV, which is attributed to the *bipy*-linker. On the other hand, peaks corresponding to Cl^- species are not present. Cl^- can thus be excluded as a charge-balancing terminal ligand at the IBU. We thus assume formate (as the decomposition product of DMF) and hydroxide ions as the required charge-balancing species and ligands at the Ru-nodes.[57] However, via 3D ED and SCXRD data, such (mostly disordered) terminal ligands are difficult to localize, and further comprehensive analysis is required, but not relevant for this publication and thus subject to future work. NMR (Figure S14),

https://doi.org/10.1021/acs.chemmater.3c01845
Chem. Mater. 2024, 36, 657−665

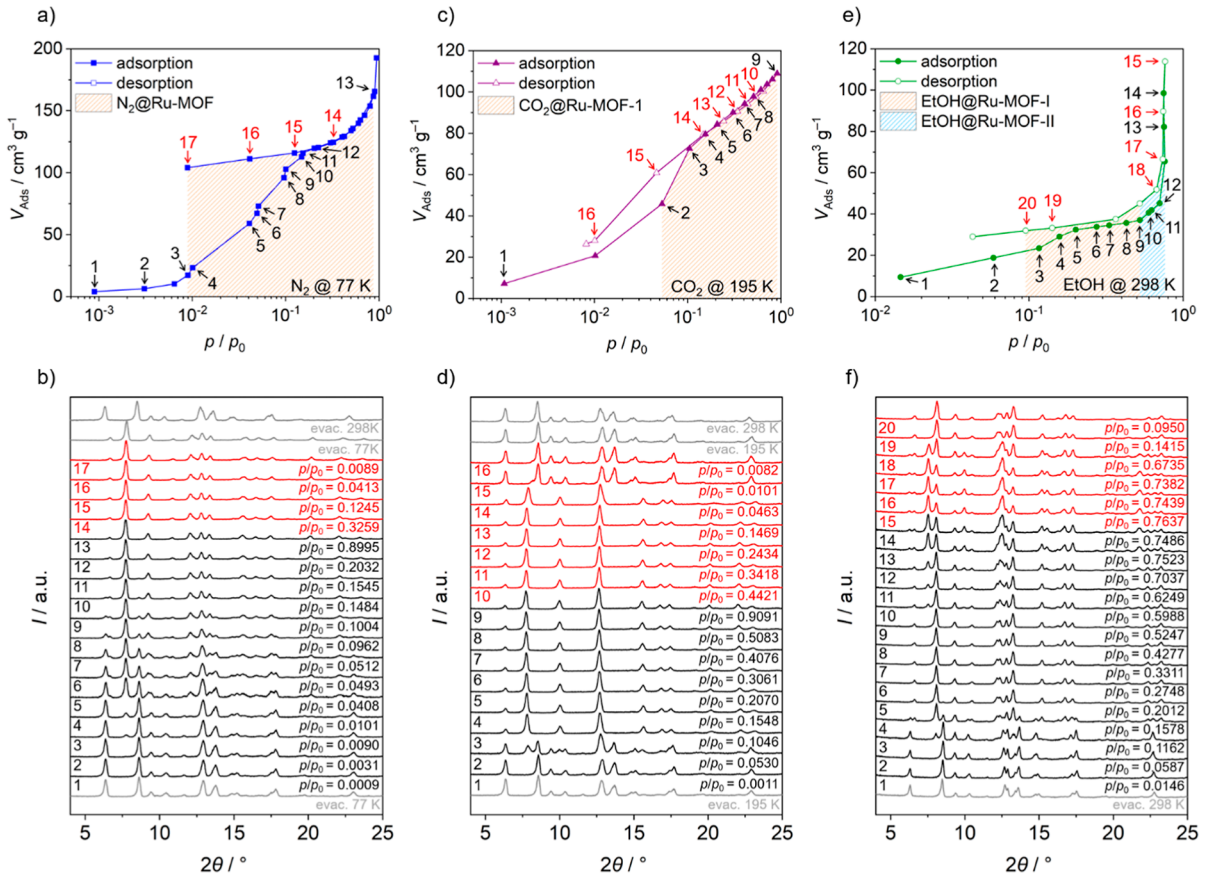

Figure 3. *In situ* PXRD study on Ru-MOF during adsorption of (a,b) N_2 (77 K); (c,d) CO_2 (195 K); and (e,f) EtOH (298 K): Physisorption isotherms [(a,c,e); semilogarithmic plots] and X-ray diffraction patterns (b,d,f) measured during adsorption (black), desorption (red), and on the evacuated sample (gray). The colors and numbers of the adsorption and desorption points correspond to the X-ray diffraction patterns. Pressure ranges in which the respective guest@Ru-MOF phases exist are marked in the isotherms by dashed areas.

IR (Figure S15), and TG measurements (Figure S16) did not allow a clear determination. Thermogravimetric analysis (TGA) was carried out in nitrogen and synthetic air (Figure S16, Supporting Information). While the oxidation of Ru-MOF in synthetic air starts at 200 °C, the material is much more stable in N_2 and pyrolyzes only above 350 °C. Both curves show only one weight loss, which indicates the decomposition of the linker molecules. Thus, trapped guests that would leave the framework at lower temperatures are not present. To determine the thermal stability, *in situ* thermo PXRD was performed between 25 and 300 °C in a nitrogen atmosphere. The diffraction patterns in Figure S17 (Supporting Information) show that loss of crystallinity and decomposition of the material are observed only at temperatures above 300 °C. Le Bail fitting of the PXRD patterns indicates a nearly linear positive volumetric thermal expansion for the framework (Figure S18, Supporting Information), reaching the value of $\alpha_V = 140\ \mu K^{-1}$. Analysis of the expansion of the specific crystallographic directions indicates an anisotropic lattice expansion, as the *a*-axis shows almost no change with increasing temperature, but the *b*- and *c*-axes increase linearly, resulting in a positive linear expansion of 77.5 and 36.4 μK^{-1}, respectively. This information points to the "soft" direction in the crystal structure and thus to the expected mechanism of guest-induced transitions in Ru-MOF.

Framework Flexibility and Sorption Properties. An apparent change in the PXRD data can be observed when Ru-MOF is desolvated or dispersed in different solvents (Figure S19, Supporting Information). This guest-induced structural transformation is reversible, and Ru-MOF reverts to the as-synthesized structure upon storage in a vacuum or under ambient conditions overnight (depending on the solvent). These findings clearly indicate the framework dynamics of guest physisorption.[8] Supramolecular porous frameworks are known to be flexible and show various reversible structural transformations.[58−61] Laminated coordination polymers can show phase transitions caused by external stimuli, either within the layer or in between the layers.[58] To confirm these assumptions, the adsorption properties of Ru-MOF were investigated for several gases. Ar (87 K) and N_2 (77 K) physisorption isotherms (Figure S20, Supporting Information) show characteristics differing compared with classical "type I" adsorption of microporous materials.[62] Both isotherms provide delayed adsorption at a relative pressure of $p/p_0 = 0.01$. Subsequently, N_2 is adsorbed in one step, while for Ar adsorption, two distinct steps can be identified before reaching a plateau (uptake at a relative pressure of 0.9 is 4.84 mmol g^{-1} for N_2 and 10.63 mmol g^{-1} for Ar). The desorption branch of the N_2 and Ar isotherms shows no steps over the whole pressure range. However, the adsorbed Ar and N_2 gas is only partially desorbed even when the pressure is reduced to 10^{-4} bar, revealing the microporous nature of the solid.[63] In general, "gating" phenomena and stepwise adsorption are typical for flexible MOFs and indicative of possible structural changes. The material starts to adsorb only above a certain threshold pressure (gate opening pressure). Transformation of a narrow pore (np) phase to an open pore (op) phase, triggered by the guest molecules, occurs and enables

https://doi.org/10.1021/acs.chemmater.3c01845
Chem. Mater. 2024, 36, 657−665

enhanced adsorption.[8] Furthermore, hysteretic loops in adsorption/desorption isotherms indicate metastable states of the MOF during adsorption/desorption. The extent of the effects depends on the material, crystal size, nature of the guest, and adsorption temperature.[64] Differences in Ar (87 K) and N_2 (77 K) adsorptions in terms of maximum uptake and isothermal shape may be due to host−guest interactions differing in magnitude. Argon as a noble gas, is considered largely inert, while nitrogen, with its quadrupole moment, can enter into strong interactions with the framework.[62] This may also lead to different structural transformation mechanisms for the flexible material. To track the structural transformation in Ru-MOF upon physisorption of guest molecules, an *in situ* PXRD investigation was performed,[49] using N_2 (77 K), CO_2 (195 K), and EtOH (298 K) as adsorptive (Figure 3). In the following, the desolvated phase will be referred to as the narrow pore (np) phase, and phases after structural transformation (adsorption) will be referred to as the open pore (op) phases. X-ray diffraction patterns were collected in parallel to N_2 adsorption/desorption in the relative pressure range $0.001 \leq p/p_0 \leq 0.9$ (Figure 3a,b). Up to $p/p_0 = 9.0 \times 10^{-3}$ Ru-MOF shows an N_2 uptake of only 17 $cm^3\ g^{-1}$. In this region, the PXRD patterns show no changes in comparison with the evacuated np phase at 77 K. A further increase in the pressure up to the gate opening pressure is accompanied by changes in the PXRD patterns: In a relative pressure range of $0.01 \leq p/p_0 \leq 0.15$, new reflections of the N_2@Ru-MOF op phase appear, while at the same time, reflections of the np phase decrease in intensity. Up to $p/p_0 = 0.15$, N_2@Ru-MOF op and np phase coexist, and the low transition rate can be explained by different nucleation times, usually explained by a broad distribution of crystallite size or surface defects.[65−67] However, when the plateau in the adsorption branch is reached, a pure op phase is observed. PXRD patterns, measured at $p/p_0 = 0.95$, were used for structure solution and refinement. In desorption, a reverse transition to the np phase cannot be observed even after applying dynamic vacuum at 77 K, indicating the strong trapping of nitrogen in micropores at 77 K. The np phase could be recovered only when heated to 298 K in a dynamic vacuum.

CO_2 adsorption was performed at 195 K (Figure 3c,d). At higher temperatures (273 or 298 K), no significant CO_2 uptake occurs in the pressure range of 0−1 bar (Figure S21, Supporting Information). The isotherm displays a characteristic comparable to that of N_2 adsorption. Gate opening occurs around $p/p_0 = 0.05$, and already at $p/p_0 = 0.10$, a CO_2@Ru-MOF op phase is present exclusively (Figure 3d). However, hysteresis is less pronounced, and gate closing occurs already at $p/p_0 = 0.01$. Thus, CO_2 is not trapped in the pores. The shift of gate opening and gate closing pressures is probably due to higher interaction energy and faster diffusion of CO_2 (compared to N_2) through the pores. Le Bail fit of *in situ* PXRDs indicates the phase coexistence of Ru-MOF and N_2@Ru-MOF-I in the pressure range of 0−20 kPa, whereas adsorption of CO_2 shows a high transition rate of switching from Ru-MOF to CO_2@Ru-MOF at 5 kPa (Figures S22 and S23, Supporting Information). Figure 2f shows X-ray diffraction patterns collected during EtOH adsorption/desorption at 298 K in the pressure range $0.015 \leq p/p_0 \leq 0.76$ and the corresponding isotherm (Figure 2e). As for Ar sorption, two steps can be observed in the adsorption branch. Ru-MOF starts to adsorb EtOH at relatively low pressures, showing "type I" behavior up to $p/p_0 = 0.12$. Analysis of the geometrical porosity of the Ru-MOF np phase indicates a non-accessible transient porosity of 0.1 $cm^3\ g^{-1}$ (Table S4, Supporting Information), which obviously can be accessed by ethanol molecules without inducing the phase transition in the solid.[68] At $p/p_0 = 0.16$, a kink in the adsorption branch and changes in PXRD mark the gate opening and phase transformation from a np to an EtOH@Ru-MOF-I phase. Phase transformation from Ru-MOF to EtOH@Ru-MOF-I phase is shifted toward higher relative pressure compared to N_2 and CO_2 experiments. In the plateau at $0.20 \leq p/p_0 \leq 0.60$, single-phase EtOH@Ru-MOF-I is observed. Further pressure increases lead to the second step in the adsorption branch, accompanied by the formation of an EtOH@Ru-MOF-II phase. Additional reflections appear in the PXRDs, indicating a gradual tilt rather than a sharp phase transformation, pointing out the low transition rate of the switching. PXRD data collection in the pressure range of $p/p_0 > 0.76$ was technically restricted because of condensation of the fluid.

Effect of Particle Size. By variation of the concentration of the synthesis solution (DMF amount), the particle size of Ru-MOF can be controlled. Thereby higher dilution leads to larger crystals as shown by SEM images (Figure S27, Supporting Information) and the color changes from green to bright yellow. PXRD patterns remain largely the same; for small particles, an increase can be observed at small 2θ values (Figure S2, Supporting Information). However, argon physisorption is largely affected by the particle size. For larger particles the gate opening starts at higher pressure (Figure S27, Supporting Information). In addition, the shape of the isotherm changes from one-to two-step adsorption. Both indicate changes in dynamic behavior depending on the particle size, which will be investigated in future work. In general, such behavior is not atypical and has already been observed in other flexible MOFs.[69−71]

Switching Mechanism. The *in situ* PXRD experiments demonstrate the dynamic properties of Ru-MOF and the structural transformation triggered by guest molecules. Thereby, the phase transition and adsorption behavior are dependent on the probe molecule. Interestingly, PXRD patterns, measured in saturation range of nitrogen (77 K), carbon dioxide (195 K), and ethanol (298 K) do not match, indicating an adsorptive dependent crystal-to-crystal phase transition (Figure S24). In order to understand the "gate opening" in Ru-MOF upon ethanol adsorption, 3D ED experiments were carried out. For this purpose, the vapor pressure of the ethanol had to be reduced so that the ultrahigh vacuum of the TEM does not cause an *in situ* phase transformation. Accordingly, an ethanol dispersion was dropped onto a TEM grid and frozen with liquid nitrogen and then transferred to the TEM (cryo-transfer). Most of the acquired 3D ED data sets were related to the Ru-MOF np phase measured at room temperature without cryo-transfer. However, in a few cases, it was possible to measure the EtOH@Ru-MOF-I phase (Figure 1b). The lattice parameters are closely related to the Ru-MOF np-phase. The lattice shrinks in the *a*-direction by roughly 13%, whereas ***b***- and especially the ***c***-direction are significantly elongated in comparison [a = 16.449(5) Å, b = 21.969(4) Å, c = 9.579(2) Å, and β = 101.05(2)°] (see Supporting Information Table S2 for more details). In addition, two other aspects were observed: (1) the Bravais lattice changes from P- to C-centering, allowing the structure to be described by fewer parameters and thus being more symmetric, and (2) no diffuse scattering is observed in the data sets of EtOH@Ru-MOF-I. The structure could be solved based on two combined 3D ED data sets solely and in principle resembles the structure of the Ru-MOF np-phase as expected (Figure 1d). However, the

https://doi.org/10.1021/acs.chemmater.3c01845
Chem. Mater. 2024, 36, 657−665

structural refinement revealed an interesting feature of the *bzpdc* linker. As can be seen in the differential potential maps (see Figure S6, Supporting Information), the carbonyl group of the linker does not seem to be confirmed but a tetrahedral geometry of the corresponding carbon atom. Either the electron beam and/or the illumination with light during the sample preparation might already trigger an excited state of the linker, which could lead to a further reaction of ethanol and other radical fragments in the pores of the Ru-MOF.[42−47] This interesting aspect will be further investigated in the following studies.

Analysis of *in situ* PXRD patterns, measured in parallel to physisorption of nitrogen at 77 K, carbon dioxide at 195 K and ethanol at 298 K suggests different structures for the guest filled phases (Figure S24, Supporting Information). Only one guest-filled phase is observed in the case of nitrogen- and carbon dioxide adsorption, whereas two phases are observed in the case of ethanol adsorption. Indexing of PXRD patterns, measured in the plateau of the corresponding isotherms suggests the *C*-centered monoclinic symmetry and unit cell constants similar to EtOH@Ru-MOF-I structure, obtained in 3D ED experiment (Table S3, Supporting Information). The structure of the second ethanol-filled phase could not be derived from PXRD unambiguously because of the tentative phase mixture of EtOH@Ru-MOF-I and EtOH@Ru-MOF-II phases. Interestingly, the EtOH@Ru-MOF-I structure, derived from *in situ* PXRD experiment, is slightly different from EtOH@Ru-MOF-I phase, obtained in the electron diffraction experiment. The reason probably lies in a photochemical reaction of the MOF in the electron beam, which is to be investigated in a subsequent work. But also, high-vacuum (required in the 3D ED experiment) and/or temperature-dependent flexibility of the EtOH@Ru-MOF structure, proved by PXRD (Figure S17, Supporting Information), are among the possible reasons for observed deviations.

Overall, a reasonable structural model of the np and op phases could be created on the basis of the 3D ED and *in situ* PXRD data. The starting structural models with corresponding unit cell parameters were simulated and subjected to Rietveld analysis (for details, see Section S2.2, Supporting Information). Detailed geometrical analysis of the crystal structures of Ru-MOF, N_2@Ru-MOF, CO_2@Ru-MOF, and EtOH@Ru-MOF shines light on the flexibility mechanism in the framework (Figure 4)

(1) Low connectivity of the metal cluster, coordinated by two carboxylates and two 4,4′-bipyridine linkers facilitates the distortion, which is reflected in the N−Ru−Ru−N angle, ranging from 144° in EtOH@Ru-MOF to 171° in N_2@Ru-MOF;

(2) The mechanism of the guest-induced switching is based mainly on the conformational flexibility of the C−C−C angle of the carbonyl moiety. In the guest-free structure, the angle is 109.4°, indicating quite large deviation from expected 120°. In the structures N_2@Ru-MOF, CO_2@Ru-MOF, and EtOH@Ru-MOF, the C−C−C angle gradually increases showing the values of 116.7, 122.4, and 128.4° (Figure 4). Variation of the angle leads to the changes in porosity. Thus, geometrical pore size distribution, calculated using Zeo++,[72] reveals the increasing of the largest pore from 6.1 Å in Ru-MOF to 6.6 Å in N_2@Ru-MOF to 7.7 Å in CO_2@Ru-MOF and 6.8 Å in EtOH@Ru-MOF (Figure S25, Supporting Information)

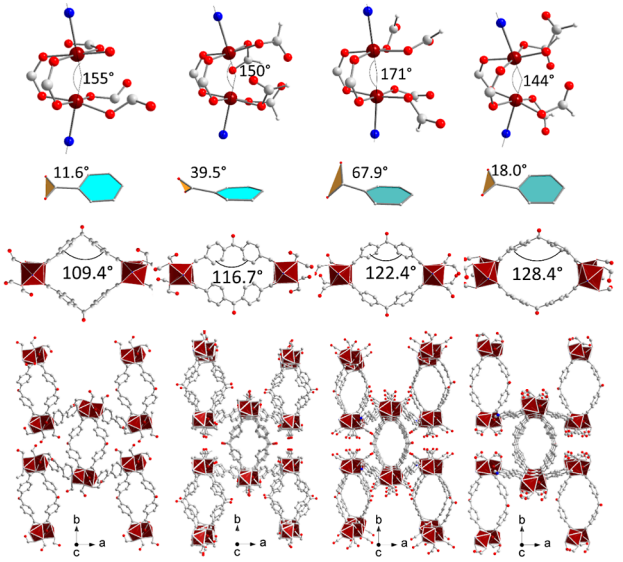

Figure 4. From top to bottom: Guest-induced transitions in Ru-MOF indicating the changes in Ru-paddle wheels; change of interplanar angles between carboxylates and phenyl rings; arrangement of *bzpdc* linkers; and packing along the 001 direction. (a) Crystal structure of desolvated Ru-MOF; (b) crystal structure of desolvated N_2@Ru-MOF; (c) crystal structure of CO_2@Ru-MOF; and (d) crystal structure of EtOH@Ru-MOF.

(3) Conformational flexibility of *bzpdc* linkers in the structure, namely the interplanar angles between carboxylates and phenyl rings. In Ru-MOF guest-free structure, the angle amounts to 11.6°. Guest-induced opening leads to change the value to 39.5° in N_2@Ru-MOF, 67.9° in CO_2@Ru-MOF and 18° for EtOH@Ru-MOF.

In summary, the interplay of the three structural features enables the crystal structure to transform, reaching an energetic minimum defined by the adsorbed guests. Interestingly, the Le Bail fit of *in situ* PXRD indicates the first-order transition in all cases with a narrow range of phase coexistence and, therefore, a high transition rate of transition (see Supporting Information Figures S22 and S23).

Finally, in addition to ethanol, vapor sorption was also performed at 298 K with water and pentane (Figure S26). Considerable differences are evident among the isotherms. While no significant uptake of water occurs, pentane and ethanol are absorbed, with higher ethanol uptake at low relative pressures. The differences are probably due to the ability of the adsorbents to trigger a structural transformation and to open the pore system. PXRDs of Ru-MOF in dispersions of water, EtOH, and pentane support this assumption (Figure S26). For water, no structural transformation can be observed; EtOH shows a complete transformation, and for pentane, both phases can be observed side by side. Thus, gate-opening is prevented for water, and compared to pentane, ethanol enables a faster np-op phase transition.

CONCLUSIONS

In this work, we designed a new multifunctional guest-responsive MOF with rare ruthenium IBUs. [Ru_2(*bzpdc*)(*bipy*)] represents a 2D structure combining unique and highly demanded material properties:

https://doi.org/10.1021/acs.chemmater.3c01845
Chem. Mater. 2024, 36, 657−665

(1) Mixed-valent ruthenium centers that can serve as a key point for catalytic and gas sorption applications.[12,55,73]
(2) Photoreactive *bzpdc*-linker molecules allow an easily accessible and versatile possibility for postsynthetic modification.[42−47] Furthermore, as benzophenone-units are among the most used photosensitizers,[74] their combination with the Ru-centers might lead to advanced (photo) catalytic properties to be tested in subsequent work.
(3) The framework of the nanoporous material exhibits reversible structural dynamics upon physisorption of guest molecules.[8] Application of *in situ* PXRD in parallel to N_2 (77 K), CO_2 (195 K), and EtOH (298 K) physisorption, the reversible guest-induced phase transitions could be traced. Transitions between a narrow pore (np) and an open pore (op) phases are adsorptive-specific. The crystal structure of EtOH@Ru-MOF was solved using 3D ED data on ethanol-incubated Ru-MOF and the structures of N_2@Ru-MOF and CO_2@Ru-MOF were refined using *in situ* PXRD data.
(4) The switching mechanism is guest-dependent and is mainly based on the variation of the C−C−C angle and the conformation of the benzophenone moiety.
(5) The "gate opening" pressure can be controlled in the range of $p/p_0 = 10^{-2} - 10^{-1}$ by variation of crystallite size of Ru-MOF in the synthesis.

In further work, we plan to investigate the applications of Ru-MOF in detail, especially the catalytic properties. The combination of guest-specific structural transformation with the reactive mixed-valent Ru centers and photoreactive *bzpdc*-linker molecules renders the material ideal as a smart switchable (photo)catalyst.

EXPERIMENTAL SECTION

Chemicals. All chemicals were used without further purification. 4,4′-Benzophenone dicarboxylic acid (95%, abcr, H_2*bzpdc*), 4,4′-bipyridine (98%, abcr, *bipy*), *N*,*N*-dimethylformamide (99.8%, Sigma-Aldrich, DMF), ethanol (absolute, EMPLURA), and ruthenium(III) chloride hydrate (99.9%, thermo scientific, $RuCl_3{\cdot}xH_2O$).

Synthesis of Ru-MOF. For the synthesis and development of Ru-MOF, a comprehensive parameter screening was necessary (for further details, see Supporting Information, Section S1.3. The investigations resulted in the following prescription for the synthesis of phase-pure Ru-MOF: 50.0 mg $RuCl_3{\cdot}xH_2O$ (0.2 mmol, 1 equiv), 15.6 mg *bipy* (0.1 mmol, 0.5 equiv), and 108.1 mg H_2*bzpdc* (0.4 mmol, 2 equiv) are added to the Teflon insert of an autoclave. 10 mL of DMF is added, and the suspension is treated for 15 min in an ultrasonic bath. The autoclaves are then sealed, and the synthesis is carried out for 72 h at 170 °C. After cooling to room temperature, the product is washed once with ethanol, once with an ethanol−water mixture (1:1), and finally again with ethanol. Between the washing steps, centrifugation is performed for 15 min (5000 rpm). The resulting bright yellow powder is allowed to dry in the air.

Optimized upscale conditions for 40 mL autoclaves are as follows: A suspension of 193.8 mg $RuCl_3{\cdot}xH_2O$ (0.78 mmol, 1 equiv), 60.55 mg *bipy* (0.39 mmol, 0.5 equiv), and 419.1 mg H_2*bzpdc* (1.55 mmol, 2 equiv) in 36 mL DMF is transferred to the Teflon insert of an autoclave and treated for 30 min in an ultrasonic bath. The synthesis is carried out for 72 h at 170 °C. After cooling to room temperature, the bright yellow product is washed and dried, as described above.

ASSOCIATED CONTENT

Supporting Information

The Supporting Information is available free of charge via the internet at. The Supporting Information is available free of charge at https://pubs.acs.org/doi/10.1021/acs.chemmater.3c01845.

Experimental part, characterization techniques, structure determination, crystal structure data and adsorption properties, additional characterization (PDF)

Crystal structure information (ZIP)

Adsorption information files (ZIP)

Animations of Ru-MOF crystal structures (ZIP)

AUTHOR INFORMATION

Corresponding Authors

Volodymyr Bon − *Chair of Inorganic Chemistry I, Technische Universität Dresden, Dresden D-01069, Germany;* orcid.org/0000-0002-9851-5031; Email: volodymyr.bon@tu-dresden.de

Yaşar Krysiak − *Institute of Inorganic Chemistry, Leibniz Universität Hannover, Hannover D-30167, Germany;* orcid.org/0000-0001-9314-8394; Email: yasar.krysiak@aca.uni-hannover.de

Authors

Karen D. J. Hindricks − *Institute of Inorganic Chemistry, Leibniz Universität Hannover, Hannover D-30167, Germany;* orcid.org/0000-0002-5549-922X

Oliver Treske − *Institute of Inorganic Chemistry, Leibniz Universität Hannover, Hannover D-30167, Germany*

Adrian Hannebauer − *Institute of Inorganic Chemistry, Leibniz Universität Hannover, Hannover D-30167, Germany;* orcid.org/0000-0003-3060-9899

Andreas Schaate − *Institute of Inorganic Chemistry, Leibniz Universität Hannover, Hannover D-30167, Germany;* orcid.org/0000-0001-7908-6553

Stefan Kaskel − *Chair of Inorganic Chemistry I, Technische Universität Dresden, Dresden D-01069, Germany;* orcid.org/0000-0003-4572-0303

Complete contact information is available at: https://pubs.acs.org/10.1021/acs.chemmater.3c01845

Notes

The authors declare no competing financial interest.

ACKNOWLEDGMENTS

This work is dedicated to Prof. Dr. Peter Behrens (†13.01.2023). K.D.J.H. thanks the Studienstiftung des Deutschen Volkes (German National Academic Foundation) for a scholarship. The authors are grateful to Lukáš Palatinus for access to the TEM FEI Tecnai 20 at the Institute of Physics of the Czech Academy of Sciences. A.H., A.S., and Y.K. acknowledge the support from the Laboratory of Nano and Quantum Engineering (LNQE). V.B. and S.K. thank the BMBF (projects nos. 05K22OD1 and 05K22OD2) for financial support. This work is funded by the Deutsche Forschungsgemeinschaft (DFG) under Germany's Excellence Strategy within the Cluster of Excellence PhoenixD (EXC 2122, project ID 390833453).

REFERENCES

(1) Cheetham, A. K.; Férey, G.; Loiseau, T. Open-Framework Inorganic Materials. *Angew. Chem., Int. Ed.* **1999**, *38* (22), 3268−3292.
(2) Ciesla, U.; Schüth, F. Ordered mesoporous materials. *Microporous Mesoporous Mater.* **1999**, *27* (2−3), 131−149.

(3) Kitagawa, S.; Kitaura, R.; Noro, S. Functional porous coordination polymers. *Angew. Chem., Int. Ed.* **2004**, *43* (18), 2334−2375.
(4) Zhou, H.-C.; Long, J. R.; Yaghi, O. M. Introduction to metal-organic frameworks. *Chem. Rev.* **2012**, *112* (2), 673−674.
(5) Long, J. R.; Yaghi, O. M. The pervasive chemistry of metal-organic frameworks. *Chem. Soc. Rev.* **2009**, *38* (5), 1213−1214.
(6) Furukawa, H.; Cordova, K. E.; O'Keeffe, M.; Yaghi, O. M. The chemistry and applications of metal-organic frameworks. *Science* **2013**, *341* (6149), 1230444.
(7) Kitagawa, S.; Uemura, K. Dynamic porous properties of coordination polymers inspired by hydrogen bonds. *Chem. Soc. Rev.* **2005**, *34* (2), 109−119.
(8) Schneemann, A.; Bon, V.; Schwedler, I.; Senkovska, I.; Kaskel, S.; Fischer, R. A. Flexible metal-organic frameworks. *Chem. Soc. Rev.* **2014**, *43* (16), 6062−6096.
(9) Evans, J. D.; Bon, V.; Senkovska, I.; Lee, H.-C.; Kaskel, S. Four-dimensional metal-organic frameworks. *Nat. Commun.* **2020**, *11* (1), 2690.
(10) Yaghi, O. M.; O'Keeffe, M.; Ockwig, N. W.; Chae, H. K.; Eddaoudi, M.; Kim, J. Reticular synthesis and the design of new materials. *Nature* **2003**, *423* (6941), 705−714.
(11) Gándara, F.; Furukawa, H.; Lee, S.; Yaghi, O. M. High methane storage capacity in aluminum metal-organic frameworks. *J. Am. Chem. Soc.* **2014**, *136* (14), 5271−5274.
(12) Murray, L. J.; Dincă, M.; Long, J. R. Hydrogen storage in metal-organic frameworks. *Chem. Soc. Rev.* **2009**, *38* (5), 1294−1314.
(13) Suh, M. P.; Park, H. J.; Prasad, T. K.; Lim, D.-W. Hydrogen storage in metal-organic frameworks. *Chem. Rev.* **2012**, *112* (2), 782−835.
(14) Li, J.-R.; Sculley, J.; Zhou, H.-C. Metal-organic frameworks for separations. *Chem. Rev.* **2012**, *112* (2), 869−932.
(15) Lee, J.; Farha, O. K.; Roberts, J.; Scheidt, K. A.; Nguyen, S. T.; Hupp, J. T. Metal-organic framework materials as catalysts. *Chem. Soc. Rev.* **2009**, *38* (5), 1450−1459.
(16) Dhakshinamoorthy, A.; Li, Z.; Garcia, H. Catalysis and photocatalysis by metal organic frameworks. *Chem. Soc. Rev.* **2018**, *47* (22), 8134−8172.
(17) Zhu, L.; Liu, X.-Q.; Jiang, H.-L.; Sun, L.-B. Metal-Organic Frameworks for Heterogeneous Basic Catalysis. *Chem. Rev.* **2017**, *117* (12), 8129−8176.
(18) Pascanu, V.; González Miera, G.; Inge, A. K.; Martín-Matute, B. Metal-Organic Frameworks as Catalysts for Organic Synthesis: A Critical Perspective. *J. Am. Chem. Soc.* **2019**, *141* (18), 7223−7234.
(19) Kreno, L. E.; Leong, K.; Farha, O. K.; Allendorf, M.; van Duyne, R. P.; Hupp, J. T. Metal-organic framework materials as chemical sensors. *Chem. Rev.* **2012**, *112* (2), 1105−1125.
(20) Naota, T.; Takaya, H.; Murahashi, S.-I. Ruthenium-Catalyzed Reactions for Organic Synthesis. *Chem. Rev.* **1998**, *98* (7), 2599−2660.
(21) Murahashi, S.-I.; Takaya, H.; Naota, T. Ruthenium catalysis in organic synthesis. *Pure Appl. Chem.* **2002**, *74* (1), 19−24.
(22) Sato, S.; Arai, T.; Morikawa, T.; Uemura, K.; Suzuki, T. M.; Tanaka, H.; Kajino, T. Selective CO2 conversion to formate conjugated with H2O oxidation utilizing semiconductor/complex hybrid photocatalysts. *J. Am. Chem. Soc.* **2011**, *133* (39), 15240−15243.
(23) Suzuki, T. M.; Tanaka, H.; Morikawa, T.; Iwaki, M.; Sato, S.; Saeki, S.; Inoue, M.; Kajino, T.; Motohiro, T. Direct assembly synthesis of metal complex-semiconductor hybrid photocatalysts anchored by phosphonate for highly efficient CO2 reduction. *Chem. Commun.* **2011**, *47* (30), 8673−8675.
(24) Duan, L.; Bozoglian, F.; Mandal, S.; Stewart, B.; Privalov, T.; Llobet, A.; Sun, L. A molecular ruthenium catalyst with water-oxidation activity comparable to that of photosystem II. *Nat. Chem.* **2012**, *4* (5), 418−423.
(25) Mari, C.; Pierroz, V.; Ferrari, S.; Gasser, G. Combination of Ru(ii) complexes and light: new frontiers in cancer therapy. *Chem. Sci.* **2015**, *6* (5), 2660−2686.
(26) Yin, J.-F.; Velayudham, M.; Bhattacharya, D.; Lin, H.-C.; Lu, K.-L. Structure optimization of ruthenium photosensitizers for efficient dye-sensitized solar cells - A goal toward a "bright" future. *Coord. Chem. Rev.* **2012**, *256* (23−24), 3008−3035.
(27) Dey, S.; Dhal, G. C. Applications of Rhodium and Ruthenium Catalysts for CO Oxidation: an Overview. *Polytechnica* **2020**, *3* (1−2), 26−42.
(28) Wei, Y.-S.; Zhang, M.; Zou, R.; Xu, Q. Metal-Organic Framework-Based Catalysts with Single Metal Sites. *Chem. Rev.* **2020**, *120* (21), 12089−12174.
(29) Lawrence, M. A. W.; Bullock, J. L.; Holder, A. A. Basic Coordination Chemistry of Ruthenium. In *Ruthenium complexes:Photochemical and biomedical applications*; Holder, A. A., Lilge, L., Browne, W. R., Lawrence, M. A. W., Bullock, J. L., Eds.; Wiley VCH, 2018; pp 25−41.
(30) Heinz, W. R.; Kratky, T.; Drees, M.; Wimmer, A.; Tomanec, O.; Günther, S.; Schuster, M.; Fischer, R. A. Mixed precious-group metal-organic frameworks: a case study of the HKUST-1 analogue RuxRh3-x(BTC)2. *Dalton Trans.* **2019**, *48* (32), 12031−12039.
(31) Moghadam, P. Z.; Li, A.; Liu, X.-W.; Bueno-Perez, R.; Wang, S.-D.; Wiggin, S. B.; Wood, P. A.; Fairen-Jimenez, D. Targeted classification of metal-organic frameworks in the Cambridge structural database (CSD). *Chem. Sci.* **2020**, *11* (32), 8373−8387.
(32) Moghadam, P. Z.; Li, A.; Wiggin, S. B.; Tao, A.; Maloney, A. G. P.; Wood, P. A.; Ward, S. C.; Fairen-Jimenez, D. Development of a Cambridge Structural Database Subset: A Collection of Metal-Organic Frameworks for Past, Present, and Future. *Chem. Mater.* **2017**, *29* (7), 2618−2625.
(33) Kozachuk, O.; Yusenko, K.; Noei, H.; Wang, Y.; Walleck, S.; Glaser, T.; Fischer, R. A. Solvothermal growth of a ruthenium metal-organic framework featuring HKUST-1 structure type as thin films on oxide surfaces. *Chem. Commun.* **2011**, *47* (30), 8509−8511.
(34) Zhang, W.; Kozachuk, O.; Medishetty, R.; Schneemann, A.; Wagner, R.; Khaletskaya, K.; Epp, K.; Fischer, R. A. Controlled SBU Approaches to Isoreticular Metal-Organic Framework Ruthenium-Analogues of HKUST-1. *Eur. J. Inorg. Chem.* **2015**, *2015* (23), 3913−3920.
(35) Noei, H.; Kozachuk, O.; Amirjalayer, S.; Bureekaew, S.; Kauer, M.; Schmid, R.; Marler, B.; Muhler, M.; Fischer, R. A.; Wang, Y. CO Adsorption on a Mixed-Valence Ruthenium Metal-Organic Framework Studied by UHV-FTIR Spectroscopy and DFT Calculations. *J. Phys. Chem. C* **2013**, *117* (11), 5658−5666.
(36) Kozachuk, O.; Luz, I.; Llabrés i Xamena, F. X.; Noei, H.; Kauer, M.; Albada, H. B.; Bloch, E. D.; Marler, B.; Wang, Y.; Muhler, M.; Fischer, R. A. Multifunctional, defect-engineered metal-organic frameworks with ruthenium centers: sorption and catalytic properties. *Angew. Chem., Int. Ed.* **2014**, *53* (27), 7058−7062.
(37) Zhang, W.; Kauer, M.; Halbherr, O.; Epp, K.; Guo, P.; Gonzalez, M. I.; Xiao, D. J.; Wiktor, C.; Liabrés i Xamena, F. X.; Wöll, C.; Wang, Y.; Muhler, M.; Fischer, R. A. Ruthenium Metal-Organic Frameworks with Different Defect Types: Influence on Porosity, Sorption, and Catalytic Properties. *Chem.—Eur. J.* **2016**, *22* (40), 14297−14307.
(38) Epp, K.; Luz, I.; Heinz, W. R.; Rapeyko, A.; Llabrés i Xamena, F. X.; Fischer, R. A. Defect-Engineered Ruthenium MOFs as Versatile Heterogeneous Hydrogenation Catalysts. *ChemCatChem* **2020**, *12* (6), 1720−1725.
(39) Ho, J.; Nord, M. T.; Stafford, J. P.; Stylianou, K. C. Ruthenium-based metal-organic framework catalyst for CO 2 fixation onto epoxides. *Catal. Sci. Technol.* **2022**, *12* (23), 6998−7002.
(40) Zhang, W.; Freitag, K.; Wannapaiboon, S.; Schneider, C.; Epp, K.; Kieslich, G.; Fischer, R. A. Elaboration of a Highly Porous RuII,II Analogue of HKUST-1. *Inorg. Chem.* **2016**, *55* (24), 12492−12495.
(41) Lan, G.; Zhu, Y.-Y.; Veroneau, S. S.; Xu, Z.; Micheroni, D.; Lin, W. Electron Injection from Photoexcited Metal-Organic Framework Ligands to Ru2 Secondary Building Units for Visible-Light-Driven Hydrogen Evolution. *J. Am. Chem. Soc.* **2018**, *140* (16), 5326−5329.
(42) Baldovi, H. G.; Krüger, M.; Reinsch, H.; Alvaro, M.; Stock, N.; Garcia, H. Transient absorption spectroscopy and photochemical reactivity of CAU-8. *J. Mater. Chem. C* **2015**, *3* (15), 3607−3613.
(43) Reinsch, H.; Krüger, M.; Marrot, J.; Stock, N. First keto-functionalized microporous Al-based metal-organic framework: Al-

(OH)(O2C-C6H4-CO-C6H4-CO2). *Inorg. Chem.* **2013**, *52* (4), 1854−1859.
(44) Mohmeyer, A.; Schaate, A.; Brechtken, B.; Rode, J. C.; Warwas, D. P.; Zahn, G.; Haug, R. J.; Behrens, P. Delamination and Photochemical Modification of a Novel Two-Dimensional Zr-Based Metal−Organic Frameworks. *Chem.—Eur. J.* **2018**, *24* (49), 12848−12855.
(45) Mohmeyer, A.; Schäfer, M.; Schaate, A.; Locmelis, S.; Schneider, A. M.; Behrens, P. Inside/Outside: Post-Synthetic Modification of the Zr-Benzophenonedicarboxylate Metal-Organic Framework. *Chem.—Eur. J.* **2020**, *26* (10), 2222−2232.
(46) Mohmeyer, A.; Schaate, A.; Hoppe, B.; Schulze, H. A.; Heinemeyer, T.; Behrens, P. Direct grafting-from of PEDOT from a photoreactive Zr-based MOF - a novel route to electrically conductive composite materials. *Chem. Commun.* **2019**, *55* (23), 3367−3370.
(47) Hindricks, K. D. J.; Schaate, A.; Behrens, P. Postsynthetic Photochemical Modification and 2D Structuring of Zr-MOF Thin Films Containing Benzophenone Linker Molecules. *Angew. Chem., Int. Ed.* **2023**, *62*, No. e202303753.
(48) Huang, Z.; Willhammar, T.; Zou, X. Three-dimensional electron diffraction for porous crystalline materials: structural determination and beyond. *Chem. Sci.* **2021**, *12* (4), 1206−1219.
(49) Bon, V.; Senkovska, I.; Wallacher, D.; Heerwig, A.; Klein, N.; Zizak, I.; Feyerherm, R.; Dudzik, E.; Kaskel, S. In situ monitoring of structural changes during the adsorption on flexible porous coordination polymers by X-ray powder diffraction: Instrumentation and experimental results. *Microporous Mesoporous Mater.* **2014**, *188*, 190−195.
(50) Liu, D.; Wan, J.; Pang, G.; Tang, Z. Hollow Metal-Organic-Framework Micro/Nanostructures and their Derivatives: Emerging Multifunctional Materials. *Adv. Mater.* **2019**, *31* (38), No. e1803291.
(51) Lee, I.; Choi, S.; Lee, H. J.; Oh, M. Hollow Metal-Organic Framework Microparticles Assembled via a Self-Templated Formation Mechanism. *Cryst. Growth Des.* **2015**, *15* (11), 5169−5173.
(52) Huang, Z.; Ge, M.; Carraro, F.; Doonan, C.; Falcaro, P.; Zou, X. Can 3D electron diffraction provide accurate atomic structures of metal-organic frameworks? *Faraday Discuss.* **2021**, *225*, 118−132.
(53) Köberl, M.; Cokoja, M.; Herrmann, W. A.; Kühn, F. E. From molecules to materials: molecular paddle-wheel synthons of macromolecules, cage compounds and metal-organic frameworks. *Dalton Trans.* **2011**, *40* (26), 6834−6859.
(54) Dilling, W. L. The Effect of Solvent on the Electronic Transitions of Benzophenone and Its o- and p-Hydroxy Derivatives. *J. Org. Chem.* **1966**, *31* (4), 1045−1050.
(55) Férey, G.; Millange, F.; Morcrette, M.; Serre, C.; Doublet, M.-L.; Grenèche, J.; Tarascon, J.-M. Mixed-valence li/fe-based metal-organic frameworks with both reversible redox and sorption properties. *Angew. Chem., Int. Ed.* **2007**, *46* (18), 3259−3263.
(56) Xie, L. S.; Sun, L.; Wan, R.; Park, S. S.; DeGayner, J. A.; Hendon, C. H.; Dincă, M. Tunable Mixed-Valence Doping toward Record Electrical Conductivity in a Three-Dimensional Metal-Organic Framework. *J. Am. Chem. Soc.* **2018**, *140* (24), 7411−7414.
(57) Fu, Y.; Yao, Y.; Forse, A. C.; Li, J.; Mochizuki, K.; Long, J. R.; Reimer, J. A.; De Paëpe, G.; Kong, X. Solvent-derived defects suppress adsorption in MOF-74. *Nat. Commun.* **2023**, *14* (1), 2386.
(58) Luo, X.-L.; Yin, Z.; Zeng, M.-H.; Kurmoo, M. The construction, structures, and functions of pillared layer metal-organic frameworks. *Inorg. Chem. Front.* **2016**, *3* (10), 1208−1226.
(59) Biradha, K.; Hongo, Y.; Fujita, M. Crystal-to-Crystal Sliding of 2D Coordination Layers Triggered by Guest Exchange. *Angew. Chem., Int. Ed.* **2002**, *41* (18), 3395−3398.
(60) Kitaura, R.; Seki, K.; Akiyama, G.; Kitagawa, S. Porous coordination-polymer crystals with gated channels specific for supercritical gases. *Angew. Chem., Int. Ed.* **2003**, *42* (4), 428−431.
(61) Maji, T. K.; Mostafa, G.; Matsuda, R.; Kitagawa, S. Guest-induced asymmetry in a metal-organic porous solid with reversible single-crystal-to-single-crystal structural transformation. *J. Am. Chem. Soc.* **2005**, *127* (49), 17152−17153.
(62) Thommes, M.; Kaneko, K.; Neimark, A. V.; Olivier, J. P.; Rodriguez-Reinoso, F.; Rouquerol, J.; Sing, K. S. Physisorption of gases, with special reference to the evaluation of surface area and pore size distribution (IUPAC Technical Report). *Pure Appl. Chem.* **2015**, *87* (9−10), 1051−1069.
(63) Humphrey, S. M.; Oungoulian, S. E.; Yoon, J. W.; Hwang, Y. K.; Wise, E. R.; Chang, J.-S. Hysteretic sorption of light gases by a porous metal-organic framework containing tris(para-carboxylated) triphenylphosphine oxide. *Chem. Commun.* **2008**, *7* (25), 2891−2893.
(64) Férey, G.; Serre, C. Large breathing effects in three-dimensional porous hybrid matter: facts, analyses, rules and consequences. *Chem. Soc. Rev.* **2009**, *38* (5), 1380−1399.
(65) Miura, H.; Bon, V.; Senkovska, I.; Ehrling, S.; Bönisch, N.; Mäder, G.; Grünzner, S.; Khadiev, A.; Novikov, D.; Maity, K.; Richter, A.; Kaskel, S. Spatiotemporal Design of the Metal-Organic Framework DUT-8(M). *Adv. Mater.* **2023**, *35* (8), No. e2207741.
(66) Hiraide, S.; Sakanaka, Y.; Kajiro, H.; Kawaguchi, S.; Miyahara, M. T.; Tanaka, H. High-throughput gas separation by flexible metal-organic frameworks with fast gating and thermal management capabilities. *Nat. Commun.* **2020**, *11* (1), 3867.
(67) Abylgazina, L.; Senkovska, I.; Engemann, R.; Ehrling, S.; Gorelik, T. E.; Kavoosi, N.; Kaiser, U.; Kaskel, S. Impact of Crystal Size and Morphology on Switchability Characteristics in Pillared-Layer Metal-Organic Framework DUT-8(Ni). *Front. Chem.* **2021**, *9*, 674566.
(68) Nikolayenko, V. I.; Castell, D. C.; Sensharma, D.; Shivanna, M.; Loots, L.; Forrest, K. A.; Solanilla-Salinas, C. J.; Otake, K.-I.; Kitagawa, S.; Barbour, L. J.; Space, B.; Zaworotko, M. J. Reversible transformations between the non-porous phases of a flexible coordination network enabled by transient porosity. *Nat. Chem.* **2023**, *15* (4), 542−549.
(69) Sakata, Y.; Furukawa, S.; Kondo, M.; Hirai, K.; Horike, N.; Takashima, Y.; Uehara, H.; Louvain, N.; Meilikhov, M.; Tsuruoka, T.; Isoda, S.; Kosaka, W.; Sakata, O.; Kitagawa, S. Shape-memory nanopores induced in coordination frameworks by crystal downsizing. *Science* **2013**, *339* (6116), 193−196.
(70) Maliuta, M.; Senkovska, I.; Thümmler, R.; Ehrling, S.; Becker, S.; Romaka, V.; Bon, V.; Evans, J. D.; Kaskel, S. Particle size-dependent flexibility in DUT-8(Cu) pillared layer metal-organic framework. *Dalton Trans.* **2023**, *52* (9), 2816−2824.
(71) Bon, V.; Busov, N.; Senkovska, I.; Bönisch, N.; Abylgazina, L.; Khadiev, A.; Novikov, D.; Kaskel, S. The importance of crystal size for breathing kinetics in MIL-53(Al). *Chem. Commun.* **2022**, *58* (75), 10492−10495.
(72) Willems, T. F.; Rycroft, C. H.; Kazi, M.; Meza, J. C.; Haranczyk, M. Algorithms and tools for high-throughput geometry-based analysis of crystalline porous materials. *Microporous Mesoporous Mater.* **2012**, *149* (1), 134−141.
(73) Corma, A.; García, H.; Llabrés i Xamena, F. X. Engineering metal organic frameworks for heterogeneous catalysis. *Chem. Rev.* **2010**, *110* (8), 4606−4655.
(74) Dormán, G.; Nakamura, H.; Pulsipher, A.; Prestwich, G. D. The Life of Pi Star: Exploring the Exciting and Forbidden Worlds of the Benzophenone Photophore. *Chem. Rev.* **2016**, *116* (24), 15284−15398.

https://doi.org/10.1021/acs.chemmater.3c01845
Chem. Mater. 2024, 36, 657−665